Scripta Materialia 197 (2021) 113790

Contents lists available at ScienceDirect

Scripta Materialia

journal homepage: www.elsevier.com/locate/scriptamat

Determining oxidation states of transition metals in molten salt corrosion using electron energy loss spectroscopy

Kaustubh Bawane[a,*], Panayotis Manganaris[a], Yachun Wang[a], Jagadeesh Sure[b], Arthur Ronne[c], Phillip Halstenberg[d,e], Sheng Dai[d,e], Simerjeet K. Gill[f], Kotaro Sasaki[b], Yu-chen Karen Chen-Wiegart[c,g], Ruchi Gakhar[h], Shannon Mahurin[d], Simon M. Pimblott[i], James F. Wishart[b], Lingfeng He[a,*]

[a] Advanced Characterization Department, Idaho National Laboratory, Idaho Falls, ID, 83415 USA
[b] Chemistry Division, Brookhaven National Laboratory, Upton, NY, 11973, USA
[c] Department of Materials Science and Chemical Engineering, Stony Brook University, Stony Brook, NY, 11794, USA
[d] Chemical Sciences Division, Oak Ridge National Laboratory, Oak Ridge, TN, 37830, USA
[e] Department of Chemistry, University of Tennessee, Knoxville, TN, 37996, USA
[f] Nuclear Science and Technology, Brookhaven National Laboratory, Upton, NY, 11973, USA
[g] National Synchrotron Light Source II (NSLS-II), Brookhaven National Laboratory, Upton, NY, 11973, USA
[h] Pyrochemistry and Molten Salt Systems Department, Idaho National Laboratory, Idaho Falls, ID, 83415, USA
[i] Nuclear Science User Facilities, Idaho National Laboratory, Idaho Falls, ID, 83415, USA

ARTICLE INFO

Article history:
Received 17 January 2021
Accepted 7 February 2021
Available online 23 February 2021

Keywords:
Molten salt corrosion
Electron energy loss spectroscopy
Oxidation state mapping
Principal component analysis
Multiple linear least squares fitting

ABSTRACT

This work utilizes electron energy loss spectroscopy (EELS) to identify oxidation state of alloying elements in Ni-based alloys after exposure to molten chloride salt systems. Pure Ni and Ni-20Cr model alloy were corroded in molten $ZnCl_2$ and KCl-$MgCl_2$ under argon atmosphere at various temperatures. Oxidation states of Cr (Cr^{3+}) and Ni (Ni^{2+}) in the molten salt after corrosion were determined by monitoring changes in the $L_{2,3}$ edges of corresponding EELS spectra. Oxidation state mapping technique using principal component analysis and multiple linear least squares fitting in HyperSpy Python package was developed.

Molten halide salts are attracting worldwide interest due to a variety of technologically important applications such as thermal energy storage, high temperature heat transfer fluids in concentrated solar power (CSP) plants [1] and molten salt reactors (MSR) [2]. Molten halide salts exhibit many appealing properties such as high heat capacity, reasonable density, high boiling points, high thermal conductivity, high chemical stability, and low vapor pressure [2-4]. Molten chloride salts are desirable due to lower cost, lower melting temperatures, and higher solubility for fissile materials in the case of nuclear applications [5,6]. However, molten halide salts remain highly corrosive towards most structural alloys [7-9]. Most structural alloys rely on the formation of a passive layer for protection against aqueous or high temperature corrosion in oxidizing atmospheres [5,8,10]. However, in molten halide salt environments, these passive layers were found to be unstable [8,9,11]. Nickel-based alloys have been identified as leading candidates for salt-facing materials owing to high corrosion resistance and good mechanical properties [12,13]. However, nickel alloys, particularly those that contain chromium, are also susceptible to corrosion through selective removal of chromium [14-21]. First-row transition metals like Ni and Cr can exist in a wide range of oxidation states [22,23]. The oxidation state of dissolved alloying elements in the molten salt can reveal corrosion reaction products. Electron energy loss near edge structure (ELNES) in transmission electron microscope (TEM) is a popular technique that can be used to characterize the oxidation state of various multivalent elements [22,24,25].

This work demonstrates electron energy loss spectroscopy (EELS) in TEM as an effective tool to study molten salt corrosion damage in structural alloys. Our previous work explored molten salt corrosion in pure Ni and Ni-20Cr model alloys after exposure to molten $ZnCl_2$ and KCl-$MgCl_2$ salts using a variety of techniques such as cyclic polarization tests, scanning transmission electron microscopy with energy dispersive spectroscopy (STEM-EDS)

* Corresponding authors.
E-mail addresses: Kaustubh.Bawane@inl.gov (K. Bawane), Lingfeng.He@inl.gov (L. He).

https://doi.org/10.1016/j.scriptamat.2021.113790
1359-6462/

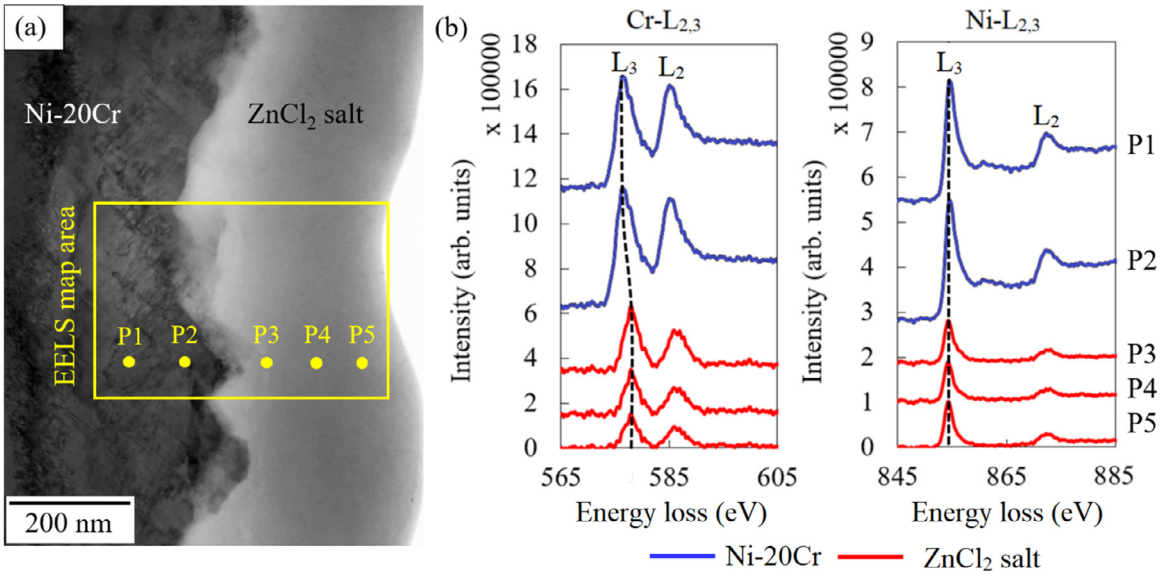

Fig. 1. (a). STEM-BF image of an interfacial cross-section of Ni-20Cr/$ZnCl_2$ after 100 h corrosion testing in molten $ZnCl_2$ [15], (b) EELS spectra showing Cr-$L_{2,3}$ and Ni-$L_{2,3}$ edges corresponding to different positions (P1-P5) in (a).

and synchrotron X-ray nanotomography [15,16]. Here, we present EELS analysis on molten salt-corroded samples under three different conditions: (1) Ni-20Cr exposed to molten $ZnCl_2$ [15], (2) pure Ni exposed to molten $ZnCl_2$ [15], (3) pure Ni exposed to molten KCl-$MgCl_2$ [16] (hereafter referred as, Ni/$ZnCl_2$, NiCr/$ZnCl_2$, and Ni/KCl-$MgCl_2$ respectively). In addition to these three samples, $CrCl_3$, $CrCl_2$ and $NiCl_2$ powder samples were also analyzed using EELS to serve as standard references for respective oxidation states of Cr and Ni elements.

TEM sample preparation on corroded samples covered with the remnant salt was performed using an in-situ lift-out technique in a field emission gun (FEG) scanning electron microscope (SEM) equipped with a focused ion beam (FIB) system (FEI Quanta 3D FEG Dual Beam) at the Center for Advanced Energy Studies (CAES). All standard reference samples were ground using a mortar and pestle and placed on a Cu grid coated with amorphous carbon. STEM-EELS 2D data array was acquired using the Thermo Scientific Talos TEM operated at 200 kV and equipped with a Gatan Imaging Filter (GIF) Quantum ER system at the Idaho National Laboratory (INL)'s Materials and Fuel Complex. The energy resolution for this system was 0.9 eV. All EELS data collection in this paper were performed using dual EELS mode with 2.5 mm diameter aperture and 0.05 eV/channel energy dispersion with core loss spectra focusing on Ni-$L_{2,3}$ and Cr-$L_{2,3}$ edges.

The background in the EELS spectrum was removed using an inverse power law fitting in the Gatan Digital Micrograph software. The L_3/L_2 integrated intensity ratio is the most popular and widely used method for the oxidation state determination of 3d transition metals. In addition to sharp L_3 and L_2 peaks, $L_{2,3}$ edges can also contain a background signal that arises from less intense transitions to continuum states [26]. L_3/L_2 integrated intensity ratios were measured using D. R. G. Mitchell's 'double arctan EELS background' script [27] in Gatan Digital Micrograph software which is based on a method developed by van Aken *et al.* [28]. In this method, two arctan functions with inflection points near the $L_{2,3}$ white lines were used to remove the continuum background in the EELS spectrum. Oxidation states of Ni and Cr in molten salt corroded samples were determined by comparing the L_3/L_2 integrated intensity ratios with standard reference samples.

Fig. 1a presents a STEM-BF image of an interfacial cross-section of the NiCr/$ZnCl_2$ sample together with the locations of the EELS measurement locations (P1-P5). The interface between the $ZnCl_2$ salt and the Ni-20Cr substrate can be clearly seen. Locations P1-P2 and P3-P5 in Fig. 1a represent the Ni-20Cr alloy and the $ZnCl_2$ salt, respectively. EELS spectra focusing on the Cr-$L_{2,3}$ and Ni-$L_{2,3}$ edges from both the salt and the metal regions are illustrated in Fig. 1b. The L_3 peak positions for the Cr-$L_{2,3}$ edges in the Ni-20Cr alloy and the $ZnCl_2$ salt are 576.33 ± 0.03 eV and 578.63 ± 0.02 eV, respectively (refer to Table 1). This indicates an energy shift to higher energy loss in the $ZnCl_2$ salt by ~2.3 eV as compared to the Ni-20Cr alloy. Whereas the energy shift in Ni-L_3 peaks between salt and metal regions of NiCr/$ZnCl_2$ sample is less than the energy resolution of EELS instrument (see Table 1). The dotted black line tracing the L_3 peak maximum for both Cr-$L_{2,3}$ and Ni-$L_{2,3}$ edges in Fig. 1b confirms the noticeable shift in the Cr-L_3 peaks as opposed to the Ni-L_3 peaks. STEM-BF image and corresponding EELS spectra of the salt and metal regions of the Ni/$ZnCl_2$ and Ni/KCl-$MgCl_2$ sample are omitted here but provided in the supplementary information for brevity (refer to Fig. S1 and S2, respectively). Similar to the NiCr/$ZnCl_2$, the Ni/$ZnCl_2$ and Ni/KCl-$MgCl_2$ samples also show a negligible energy shift in the Ni-L_3 peaks (see Table 1). The presence of apparent Ni-$L_{2,3}$ and Cr-$L_{2,3}$ edges in the salt regions of the respective molten salt corroded samples indicates leaching of both Ni and Cr alloying elements from the Ni/Ni-20Cr substrates during corrosion.

Fig. 2a and 2b shows the EELS spectra of the standard reference samples with different oxidation states for Cr and Ni, respectively. The EELS spectra of metallic Cr and Ni (oxidation state = 0) are obtained from the pristine Ni-20Cr sample. The Cr-L_3 and Ni-L_3 peak positions in the standard reference samples studied in this work and from the literature are listed in Table 2. The Cr-L_3 peak positions shift to higher energy losses for Cr^{2+} and Cr^{3+} by 1.5 eV and 2.3 eV as compared to the Cr^0 oxidation state, respectively. However, the energy shift between the Cr^{2+} and Cr^{3+} oxidation states is negligible (0.8 eV < energy resolution ~0.9 eV). The dotted line in Fig. 2a clearly illustrates energy shifts with increasing oxidation states in Cr. The NiCr/$ZnCl_2$ sample also shows an energy shift to higher energy losses for the Cr-L_3 peak in the salt region as discussed in the previous paragraph (see Fig 1b). This means that Cr in the salt region of NiCr/$ZnCl_2$ exists in a higher oxidation state and not in the metallic state. Fig. 2b shows EELS spectra of Ni and $NiCl_2$ standard reference samples. As shown in Table 2 and the dot-

Table 1
L_3 peak maxima (in eV) of Cr-$L_{2,3}$ and Ni-$L_{2,3}$ edges in molten salt-corroded samples.

Elements	Cr-$L_{2,3}$			Ni-$L_{2,3}$		
Materials	Salt region	Metal region	ΔE	Salt region	Metal region	ΔE
Ni/$ZnCl_2$	–	–	–	854.18 ± 0.03	854.28 ± 0.02	0.1
NiCr/$ZnCl_2$	578.63 ± 0.02	576.33 ± 0.03	2.3	854.33 ± 0.02	854.55 ± 0.01	0.22
Ni/KCl-$MgCl_2$	–	–	–	855.0 ± 0.1	854.8 ± 0.1	0.2

Table 2
L_3 peak maxima (in eV) of Cr and Ni in different oxidation states in standard references.

Oxidation state	Standard reference	This study	Literature
Cr0	Pristine Ni-20Cr	576.33 ± 0.03	575.5 [33]
Cr^{2+}	$CrCl_2$ powders	577.80 ± 0.80	577.11 ± 0.40 [22]
Cr^{3+}	$CrCl_3$ powders	578.60 ± 0.10	578.13 ± 0.20 [22]
Ni^0	Pristine Ni-20Cr	854.55 ± 0.01	853.4 [34]
Ni^{2+}	$NiCl_2$ powders	854.70 ± 0.20	No literature for $NiCl_2$ NiO ~ 853.6 [34]

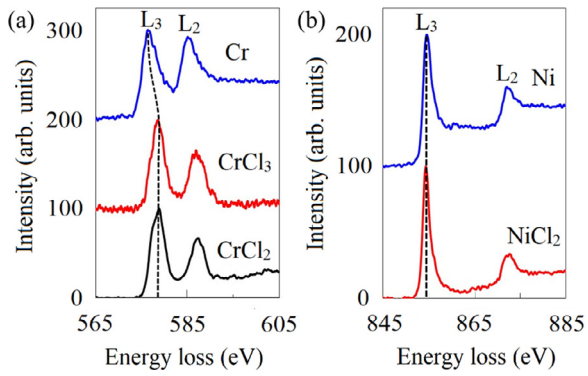

Fig. 2. Reference EELS spectra for (a) Cr-$L_{2,3}$ edges in Cr, $CrCl_3$ and $CrCl_2$ and (b) Ni-$L_{2,3}$ edges in Ni and $NiCl_2$.

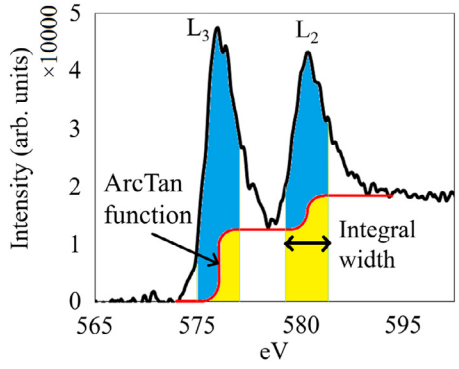

Fig. 3. Method for continuum background removal using the double arctangent function and L_3/L_2 integrated intensity ratio measurements.

ted line tracing the Ni-L_3 edge in Fig. 2b, the energy shift between Ni^0 and Ni^{2+} is negligible (~0.15 eV). This means that for Ni and Cr, the chemical shift alone cannot be used to determine the exact oxidation states of unknown samples. Many researchers have in general observed a shift to higher energy losses with increasing oxidation state [22,29-32]. This behavior is consistent with current observations involving a noticeable shift to higher energy losses for the Cr-L_3 peak with increased oxidation state. The comparison with literature data collected using instruments with different calibrations and drift tube stability adds to the uncertainty in determining the absolute chemical shift [25].

The oxidation states of transition elements can be determined by comparing the L_3/L_2 integrated intensity ratio (hereafter, referred as L_3/L_2 ratio) in $L_{2,3}$ edges of unknown samples with standard reference samples. The method used for continuum background removal and calculation of L_3/L_2 ratios with different integral widths is shown in Fig. 3. Fig. 4a shows the comparison between the L_3/L_2 ratios for the Cr-$L_{2,3}$ edges of molten salt-corroded NiCr/$ZnCl_2$ and standard reference samples as a function of integral widths (4, 6 and 8 eV). Fig. 4a indicates a reasonable match between the L_3/L_2 ratio of Cr-$L_{2,3}$ edges in $ZnCl_2$ salt region and standard reference for the Cr^{3+} oxidation state. The L_3/L_2 ratios for Cr-$L_{2,3}$ edges show negligible to marginal dependence on integral widths. Unsurprisingly, the L_3/L_2 ratios for the Cr-$L_{2,3}$ edges in Ni-20Cr region match well with the standard reference for the Cr^0 oxidation state. L_3/L_2 ratios as a function of integral width for the Ni-$L_{2,3}$ edges in NiCr/$ZnCl_2$ are shown in Fig. 4b. The L_3/L_2 ratios of salt and metal regions of NiCr/$ZnCl_2$ match well with standard reference samples for Ni^{2+} and Ni^0, respectively. The L_3/L_2 ratios for Ni^{2+} oxidation states show considerable dependence on integral widths used for the measurement. As shown in Fig. 4b, at smaller integral widths (4 eV), it is difficult to determine the oxidation state. However, L_3/L_2 ratio measurements using subsequent integral widths (6 and 8 eV) unequivocally differentiate between Ni^0 and Ni^{2+} oxidation states. Both Ni/$ZnCl_2$ and Ni/KCl-$MgCl_2$ also show Ni^{2+} in the salt region and Ni^0 in the metal region, similar to the NiCr/$ZnCl_2$ sample as shown in supplementary information (see Fig. S3). Unlike the chemical shift, the L_3/L_2 ratio method undoubtedly confirm leaching of Ni and Cr in the form of Ni^{2+} and Cr^{3+} during molten salt corrosion.

Many researchers have found that the relationship between the L_3/L_2 ratio and oxidation states can be different for various transition elements and there is no general rule [22,25,35]. For example, Schmid et al. [35] found that with increasing oxidation state, the L_3/L_2 ratio decreases for Mn and increases for Fe. Tan et al. [25] found strong correlation between the L_3/L_2 ratio and the integral width for Mn^{2+} but marginal dependence for Mn^{3+} and Mn^{4+}. Daulton et al. [22] showed an increase in the L_3/L_2 ratio from Cr^0 to Cr^{2+} and decrease from Cr^{2+} to Cr^{3+} oxidation states. This behavior agrees well with the L_3/L_2 ratio for Cr-$L_{2,3}$ edges in this manuscript which shows the highest L_3/L_2 ratio for Cr^{2+} followed by Cr^{3+} and Cr^0 as shown in Fig. 4a. For Cr, the L_3/L_2 ratio is higher in the oxidized states (Cr^{2+}/Cr^{3+}) as compared to the metallic state (Cr^0). In contrast, the L_3/L_2 ratio for the Ni-$L_{2,3}$ edges in the Ni^{2+} state is lower than the metallic state (Ni^0) as shown in Fig. 4b.

Alternatively, the oxidation states of the molten salt-corroded samples were also confirmed by comparing the shapes of their EELS spectra with standard reference spectra of metals and salts. The multiple linear least square (MLLS) technique was used to quantify differences in the EELS peak shapes. In MLLS technique, unknown EELS spectrum can be expressed as linear combination of standard references spectra as per Eq. 1. The procedure to calcu-

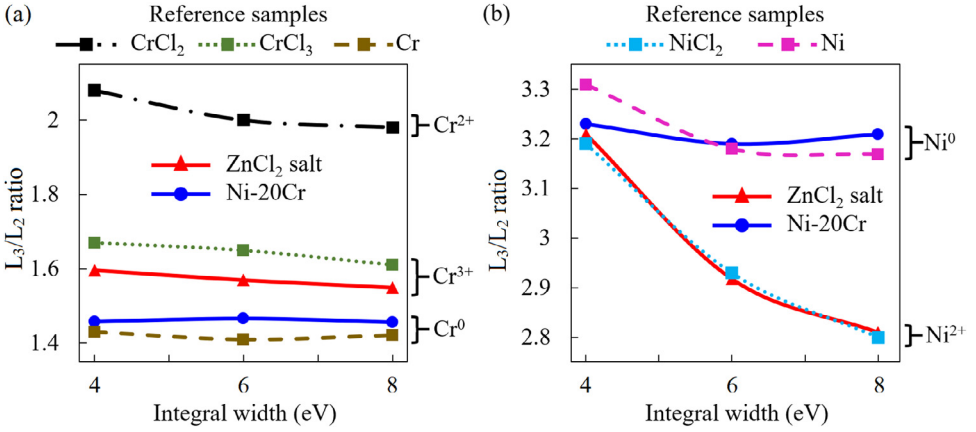

Fig. 4. L_3/L_2 integrated intensity ratios for (a) Cr-$L_{2,3}$ and (b) Ni-$L_{2,3}$ edges for $ZnCl_2$ salt, Ni-20Cr substrate and reference samples.

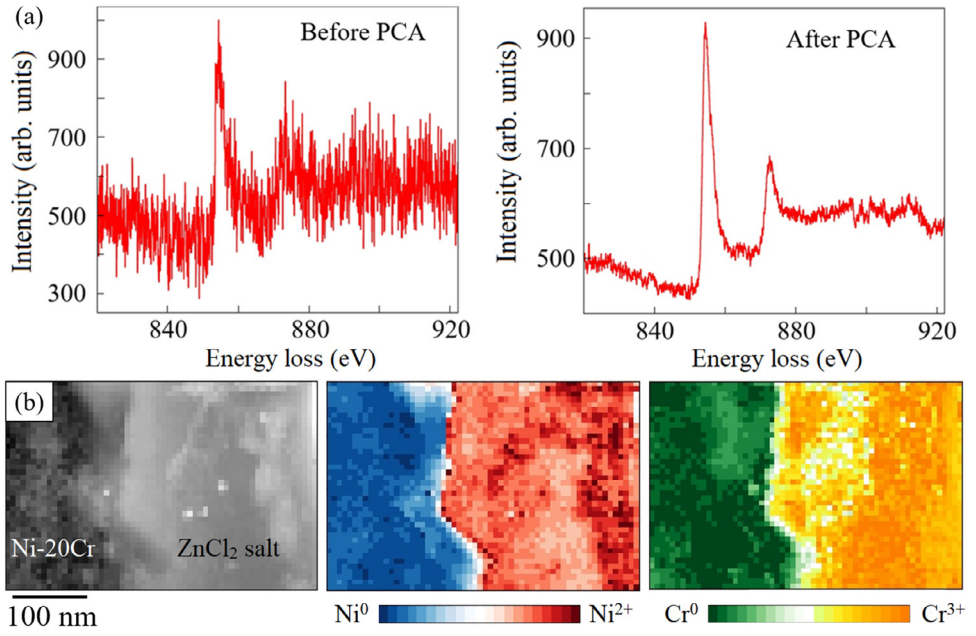

Fig. 5. (a) PCA denoising demonstrated using sample Ni-$L_{2,3}$ (b) EELS map showing chemical states of Ni and Cr at an interfacial cross-section of Ni-20Cr/$ZnCl_2$.

late % match between unknown EELS spectrum and standard reference spectra is given in Eqs. 2-5. MLLS analysis provides a very efficient and fully automated tool to characterize the oxidation states of Ni and Cr in the microstructure of metal-salt interface. Oxidation state maps of metal-salt interfaces can provide spatial distributions of different dissolved alloying elements with different oxidation states. The MLLS technique can allow oxidation state mapping by calculating % match between EELS spectrum from every pixel of 2D EELS dataset with standard references spectra. Since EELS spectra at single pixel is very noisy, principal component analysis (PCA) technique was applied to denoise the spectra before applying MLLS matching. A new, denoised EELS dataset was constructed using the largest 7 out total 20 components analyzed. Fig. 5a compares sample EELS spectrum from single pixel showing Ni-$L_{2,3}$ edges before and after PCA denoising. The oxidation state maps were constructed by plotting heat map of % match values obtained using MLLS analysis at every pixel of EELS spectrum image as shown in Fig. 5b. The maps in Fig. 5b clearly identify the interface between the metal and the salt regions of NiCr/$ZnCl_2$ and confirm the presence of Cr^0/Ni^0 and Cr^{3+}/Ni^{2+} oxidation states, respectively. These results are in good agreement with oxidation state determination using the L_3/L_2 ratio described in the previous section. Such maps are important because they can directly complement quantitative elemental maps obtained using EDS techniques. All this analysis was performed by writing a custom script that combines PCA and MLLS technique in the Jupyter Notebook application of the Anaconda software [36] with HyperSpy utilities module in Python 3. MatPlotLib module was used to visualize oxidation state maps using various colors for different oxidation states in the microstructure.

$$Y = a1.(Standard\ reference\ salt\ or\ X1) + a2.(Standard\ reference\ metal\ or\ X2) \quad (1)$$

$$Y = A.X = [a1, a2]\left[\frac{X1}{X2}\right] \quad (2)$$

$$YX' = A.X.X' \quad (3)$$

$$A = Y.X'.Inv\left(X.X'\right) \quad (4)$$

$$\%Match\ with\ standard\ reference\ salt = \frac{a1}{a1 + a2} \times 100 \quad (5)$$

Y = EELS spectrum of unknown sample
X = Matrix of standard reference EELS spectra
A = Matrix of coefficients a1 and a2
X' = Transpose of standard reference matrix
Inv() = Inverse of the matrix

Our previous work [15,16] on Ni/$ZnCl_2$, NiCr/$ZnCl_2$ and Ni/KCl-$MgCl_2$ suggested reaction mechanisms involving Cr dissolution to form both Cr^{2+} and Cr^{3+} and Ni dissolution to form Ni^{2+}. However, the current EELS results demonstrate that leaching of Cr predominantly produces Cr^{3+}. It should be noted that the formation of Cr^{2+} cannot be excluded because of the localized nature of EELS analysis. Also, the possibility of Cr^{2+} formation only during the early stages of corrosion cannot be excluded. Future corrosion studies using in-situ TEM with EELS capabilities can shed light on molten salt corrosion mechanisms by recording changes in oxidation state not only spatially, but also in real time. The present work using the HyperSpy package for Python provides strong groundwork and reliable data analysis and visualization capability to handle large in-situ EELS datasets combined with automated data processing, machine learning techniques and generation of oxidation state maps in real-time.

To summarize, the oxidation states of constituent elements (Ni and Cr) in molten salt corroded pure Ni and Ni-20Cr alloy were studied by analyzing changes in $L_{2,3}$ edges using three different methods: chemical shift investigation, L_3/L_2 integrated intensity ratios and MLLS fitting. Relying solely on the chemical shift was found to be insufficient to determine the precise oxidation states of both Cr and Ni. The L_3/L_2 integrated intensity ratio and MLLS techniques successfully identified the presence of Cr^{3+} and Ni^{2+} in the salt region and Cr^0 and Ni^0 in the metal region of molten salt-corroded microstructures. The MLLS technique was found to be far more efficient than the L_3/L_2 technique. The combination of PCA denoising using the HyperSpy package for Python with the MLLS technique was used to generate oxidation state maps as a novel way to visualize molten salt corrosion damage.

Declaration of Competing Interest

The authors declare that they have no known competing financial interests or personal relationships that could have appeared to influence the work reported in this paper.

The authors declare the following financial interests/personal relationships which may be considered as potential competing interests:

Acknowledgments

This work was supported as part of the Molten Salts in Extreme Environments Energy Frontier Research Center, funded by the U.S. Department of Energy, Office of Science. Brookhaven National Laboratory, Idaho National Laboratory, and Oak Ridge National Laboratory are operated under DOE contracts DESC0012704, DE-AC07-05ID14517, and DE-AC05-00OR22725, respectively. The authors also acknowledge the U.S. Department of Energy, Office of Nuclear Energy under DOE Idaho Operations Office Contract DE-AC07-051D14517, for use of the resources as part of Nuclear Science User Facilities. This research used resources of the National Synchrotron Light Source II, a U.S. Department of Energy (DOE) Office of Science User Facility operated for the DOE Office of Science by Brookhaven National Laboratory under Contract No. DE-SC0012704. The authors thank Megha Dubey, Jatuporn Burns, Yaqiao Wu, and Kristi Moser-McIntire at the Center for Advanced Energy Studies, and Miles Cook, Jayson Bush, Jeffery Bailey, and JoAnn Merrill at Idaho National Laboratory for their invaluable assistance.

Supplementary materials

Supplementary material associated with this article can be found, in the online version, at doi:10.1016/j.scriptamat.2021.113790.

References

[1] S. Ushak, A.G. Fernández, M. Grageda, L.F. Cabeza, in: Advances in Thermal Energy Storage Systems, Woodhead Publishing, 2015, pp. 49–63.
[2] C. Le Brun, J Nucl Mater 360 (1) (2007) 1–5.
[3] K. Vignarooban, X. Xu, K. Wang, E.E. Molina, P. Li, D. Gervasio, A.M. Kannan, Appl Energ 159 (2015) 206–213.
[4] D.F. Williams, Assessment of Candidate Molten Salt Coolants for the NGNP/NHI Heat-Transfer Loop, Oak Ridge National Laboratory Oak Ridge, TNUSA, 2006 37831.
[5] P. Sabharwall, D. Clark, M. Glazoff, G. Zheng, K. Sridharan, M. Anderson, Nucl Eng Des 280 (2014) 42–56.
[6] E.S. Sooby, A.T. Nelson, J.T. White, P.M. McIntyre, J Nucl Mater 466 (2015) 280–285.
[7] V. Ignatiev, A. Surenkov, P. Yvon, Structural Materials for Generation IV Nuclear Reactors, Woodhead Publishing (2017) 153–189.
[8] S.S. Raiman, S. Lee, J Nucl Mater 511 (2018) 523–535.
[9] Corrosion in molten salts in K. Sridharan, T.R. Allen, F. Lantelme, H. Groult, in: Elsevier, 2013, pp. 241–267.
[10] S. Guo, J. Zhang, W. Wu, W. Zhou, Prog Mater Sci 97 (2018) 448–487.
[11] C. Edeleanu, R. Littlewood, Electrochim Acta 3 (3) (1960) 195–207.
[12] M. Sarvghad, S. Delkasar Maher, D. Collard, M. Tassan, G. Will, T.A. Steinberg, Energy Storage Materials 14 (2018) 179–198.
[13] R.N. Wright, T.L. Sham, Status of metallic structural materials for molten salt reactors, Idaho National Laboratory, Idaho Falls, Idaho, 2018 83415.
[14] J.W. Koger, M.G. Fontana, R.W. Staehle, in: Advances in Corrosion Science and Technology, 4, Springer US, Boston, MA, 1974, pp. 245–318.
[15] S. Gill, J. Sure, Y. Wang, B. Layne, L. He, S. Mahurin, J. Wishart, K. Sasaki, Corros Sci 179 (2021) 109125.
[16] A. Ronne, L. He, D. Dolzhnikov, Y. Xie, M. Ge, P. Halstenberg, Y. Wang, B.T. Manard, X. Xiao, W.K. Lee, K. Sasaki, S. Dai, S.M. Mahurin, Y.K. Chen-Wiegart, ACS Appl Mater Inter 12 (15) (2020) 17321–17333.
[17] J.W. Ambrosek, Molten chloride salts for heat transfer in nuclear systems, Department of Engineering Physics, University of Wisconsin, Madison, Madison, Wisconsin, 2011.
[18] G. Zheng, K. Sridharan, JOM 70 (8) (2018) 1535–1541.
[19] L. Olson, K. Sridharan, M. Anderson, T. Allen, Mater High Temp 27 (2) (2014) 145–149.
[20] H. Sun, J. Wang, Z. Li, P. Zhang, X. Su, Solar Energy 171 (2018) 320–329.
[21] H. Sun, P. Zhang, J. Wang, Corros Sci 143 (2018) 187–199.
[22] T.L. Daulton, B.J. Little, Ultramicroscopy 106 (7) (2006) 561–573.
[23] H. Wang, S.M. Butorin, A.T. Young, J. Guo, J Phys Chem C 117 (47) (2013) 24767–24772.
[24] J.H. Paterson, O.L. Krivanek, Ultramicroscopy 32 (4) (1990) 319–325.
[25] H. Tan, J. Verbeeck, A. Abakumov, G. Van Tendeloo, Ultramicroscopy 116 (2012) 24–33.
[26] D.H. Pearson, C.C. Ahn, B. Fultz, Phys Rev B 47 (14) (1993) 8471–8478.
[27] D.R.G. Mitchell. Double Atan EELS background, 20150402, v2.0, Available from: http://www.dmscripting.com/double_atan_eels_background.html
[28] P.A. van Aken, B. Liebscher, Phys Chem Miner 29 (3) (2002) 188–200.
[29] J.H. Rask, B.A. Miner, P.R. Buseck, Ultramicroscopy 21 (4) (1987) 321–326.
[30] T. Riedl, T. Gemming, W. Gruner, J. Acker, K. Wetzig, Micron 38 (3) (2007) 224–230.
[31] J. Taftø, O.L. Krivanek, Phys Rev Lett 48 (8) (1982) 560–563.
[32] L.A.J. Garvie, A.J. Craven, R. Brydson, Am Mineral 79 (5-6) (1994) 411–425.
[33] R.D. Leapman, L.A. Grunes, P.L. Fejes, Phys Rev B 26 (2) (1982) 614–635.
[34] P.L. Potapov, D. Schryvers, Ultramicroscopy 99 (1) (2004) 73–85.
[35] H.K. Schmid, W. Mader, Micron 37 (5) (2006) 426–432.
[36] Anaconda Software Distribution. Computer software, Vers. 2-2.4.0. Anaconda, Nov. 2016 Web. <https://anaconda.com>).

Supplementary materials for:

Determining Oxidation States of Transition Metals in Molten Salt Corrosion using Electron Energy Loss Spectroscopy

Kaustubh Bawane[a,*], Panayotis Manganaris[a], Yachun Wang[a], Jagadeesh Sure[b], Arthur Ronne[c], Phillip Halstenberg[d,e], Sheng Dai[d,e], Simerjeet K. Gill[f], Kotaro Sasaki[b], Yu-chen Karen Chen-Wiegart[c,g], Ruchi Gakhar[h], Shannon Mahurin[d], Simon M. Pimblott[i], James F. Wishart[b], Lingfeng He[a,*]

[a]Advanced Characterization Department, Idaho National Laboratory, Idaho Falls, ID, 83415 USA

[b]Chemistry Division, Brookhaven National Laboratory, Upton, NY, 11973, USA

[c]Department of Materials Science and Chemical Engineering, Stony Brook University, Stony Brook, NY, 11794, USA

[d]Chemical Sciences Division, Oak Ridge National Laboratory, Oak Ridge, TN, 37830, USA

[e]Department of Chemistry, University of Tennessee, Knoxville, TN, 37996, USA

[f]Nuclear Science and Technology, Brookhaven National Laboratory, Upton, NY, 11973, USA

[g]National Synchrotron Light Source II (NSLS-II), Brookhaven National Laboratory, Upton, NY, 11973, USA

[h]Pyrochemistry and Molten Salt Systems Department, Idaho National Laboratory, Idaho Falls, ID, 83415, USA

[i]Nuclear Science User Facilities, Idaho National Laboratory, Idaho Falls, ID, 83415, USA

*Corresponding authors

E-mail address: Kaustubh.Bawane@inl.gov; Lingfeng.He@inl.gov

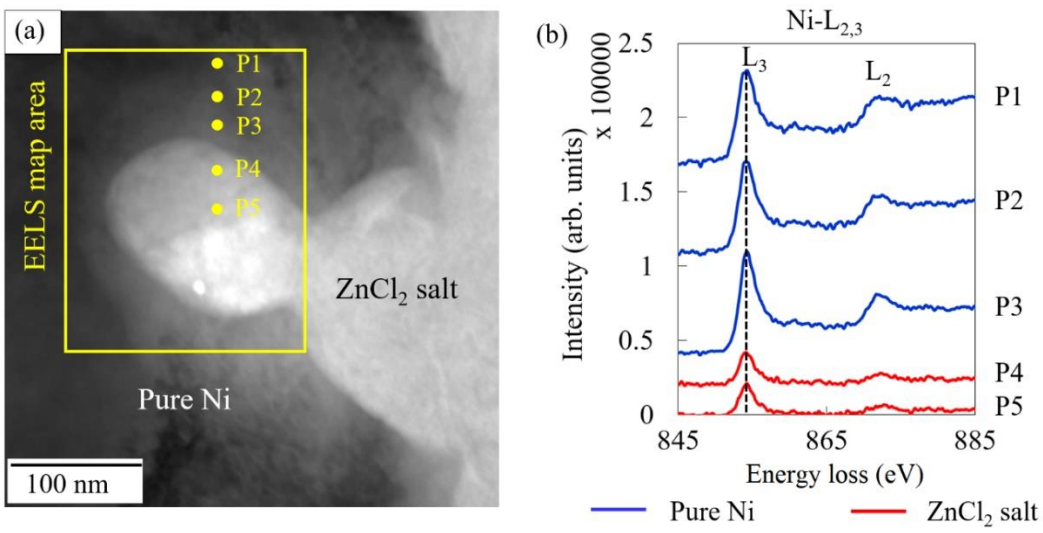

Fig. S1. (a) STEM-BF image of an interfacial cross-section of pure-Ni/$ZnCl_2$ after 100 h corrosion testing in molten $ZnCl_2$, (b) EELS spectra showing Ni-$L_{2,3}$ corresponding to different positions (P1-P5) in (a).

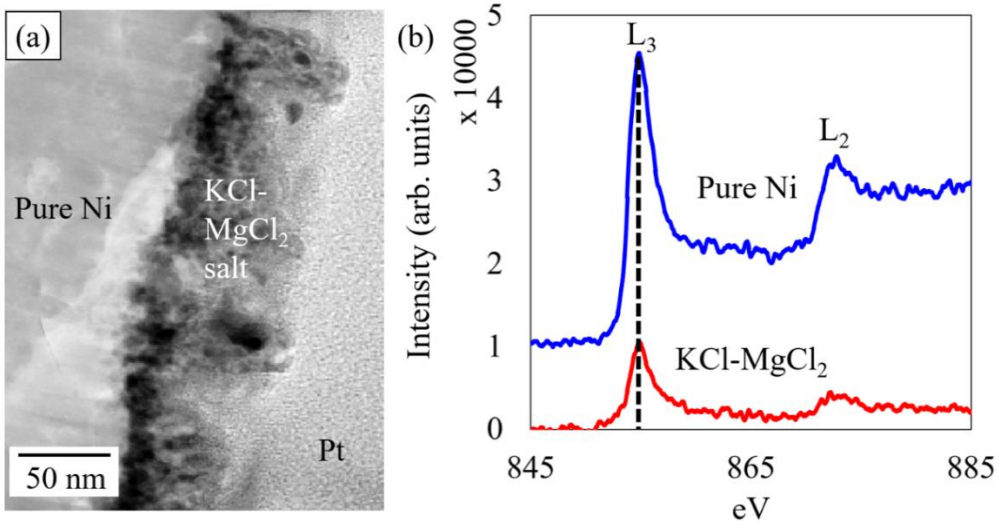

Fig. S2. (a) STEM-DF image of the pure Ni alloy after corrosion in molten KCl-$MgCl_2$ salt, (b) EELS spectra showing Ni-$L_{2,3}$ edges in the salt and metal regions.

Fig. S1a shows a STEM-bright field (BF) image of an interfacial cross-section of the Ni/$ZnCl_2$ sample. The microstructure reveals penetration of $ZnCl_2$ salt into the metallic Ni after corrosion in molten $ZnCl_2$. EELS spectra focusing on Ni-$L_{2,3}$ edges recorded at different locations

of the microstructure (P1-P5) are shown in Fig. S1b. Locations P1-P3 correspond to pure Ni and P4-P5 represent $ZnCl_2$ as shown in Fig. S1a. Fig. S2a shows a STEM-dark field (DF) image of the Ni/KCl-$MgCl_2$ sample, showing pure Ni and KCl-$MgCl_2$ salt regions and the interface between them. Fig. S2b shows the EELS spectra focusing on Ni-$L_{2,3}$ edges corresponding to the metal and salt regions. The straight dotted line tracing the Ni-L_3 peak maxima in both Fig. S1b and Fig. S2b indicates a negligible energy shift between the EELS spectra for the Ni/$ZnCl_2$ and Ni/KCl-$MgCl_2$, respectively.

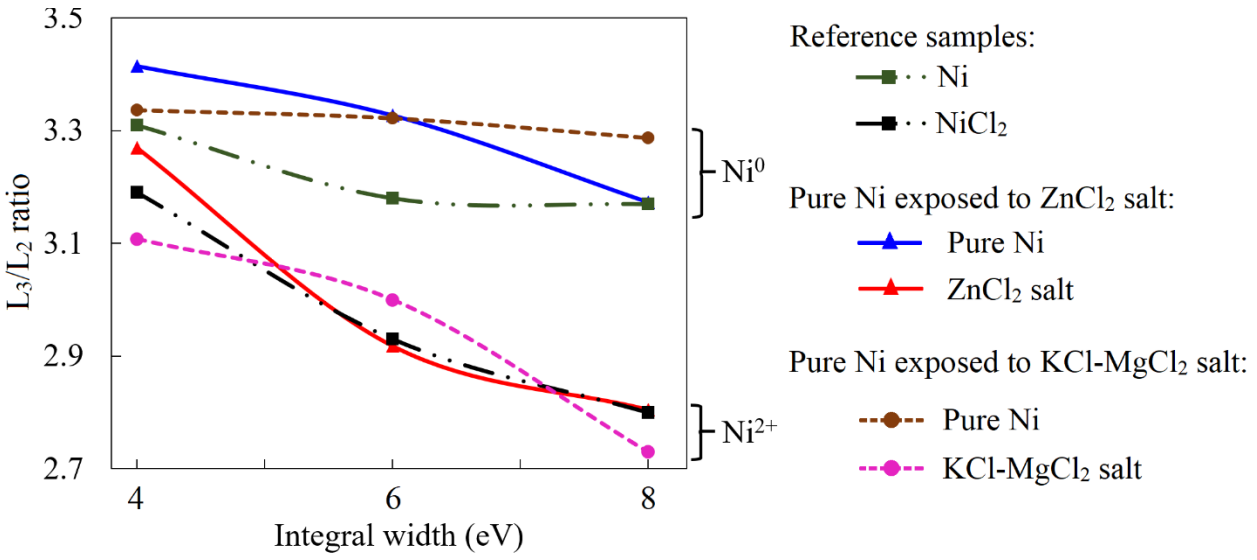

Fig. S3. L_3/L_2 ratios for Ni-$L_{2,3}$ edges for pure Ni exposed to $ZnCl_2$ or KCl-$MgCl_2$ salt in comparison with reference Ni and $NiCl_2$ samples.

Fig. S3 presents L_3/L_2 integrated intensity ratios for the Ni-$L_{2,3}$ edges of molten salt-corroded Ni/$ZnCl_2$ and Ni/KCl-$MgCl_2$ samples, in comparison with standard reference samples for the Ni^0 and Ni^{2+} oxidation states. Similar to the NiCr/$ZnCl_2$ (see Fig 4b in the main text), the L_3/L_2 ratios from salt regions in both the Ni/$ZnCl_2$ and Ni/KCl-$MgCl_2$ samples show a strong dependence on the integral width. Fig S3 confirms that both the Ni/$ZnCl_2$ and Ni/KCl-$MgCl_2$ samples show the presence of Ni^0 and Ni^{2+} oxidation states in the metal and salt regions, respectively.